Integrating Incidence Angle Dependencies Into the Clustering-Based Segmentation of SAR Images

Anca Cristea, Jeroen van Houtte, and Anthony P. Doulgeris, *Senior Member, IEEE*

***Abstract*—Synthetic aperture radar systems perform signal acquisition under varying incidence angles and register an implicit intensity decay from near to far range. Owing to the geometrical interaction between microwaves and the imaged targets, the rates at which intensities decay depend on the nature of the targets, thus rendering single-rate image correction approaches only partially successful. The decay, also known as the incidence angle effect, impacts the segmentation of wide-swath images performed on absolute intensity values. We propose to integrate the target-specific intensity decay rates into a nonstationary statistical model, for use in a fully automatic and unsupervised segmentation algorithm. We demonstrate this concept by assuming Gaussian distributed log-intensities and linear decay rates, a fitting approximation for the smooth systematic decay observed for extended flat targets. The segmentation is performed on Sentinel-1, Radarsat-2, and UAVSAR wide-swath scenes containing open water, sea ice, and oil slicks. As a result, we obtain segments connected throughout the entire incidence angle range, thus overcoming the limitations of modeling that does not account for different per-target decays. The model simplicity also allows for short execution times and presents the segmentation approach as a potential operational algorithm. In addition, we estimate the log-linear decay rates and examine their potential for a physical interpretation of the segments.**

***Index Terms*—Image segmentation, sea ice, synthetic aperture radar (SAR).**

I. Introduction

SYNTHETIC aperture radar (SAR) is used for a broad scope of observations, both from satellite and airborne platforms. The SAR imaging modality involves side-looking geometry and the acquisition of backscattered signals under varying incidence angles. As a result of the incidence angle-dependent interaction between microwaves and the imaged targets, the amount of backscattered energy decreases from near to far range, a phenomenon known as the incidence angle effect. The backscatter gradient becomes particularly noticeable in the case of wide-swath scenes, which cover hundreds of kilometers over large ranges of incidence angles ($>20^\circ$). Owing to differences in the physical properties of the targets, the effect also has a local character, which further complicates image interpretation by both human observers and algorithms. Advanced algorithms often rely on statistical representations of the backscattered signals, which currently do not account for the incidence angle effect. This work proposes to address this issue by demonstrating that incorporating a functional form of the effect into the statistical model is feasible, and that using the model for segmentation can significantly improve results.

Studies of specific backscatter dependencies with incidence angle have been conducted in the past approximately four decades for a variety of areas such as oceans, sea ice, forests, or agricultural terrain (see [1]–[4]). In many cases, especially when dealing with flat terrain and dominant surface scattering, a direct relationship between the backscattered intensity and the incidence angle can be found and even measured for different polarizations (see [5]–[7]). The empirically observed average decay rates have sometimes been approximated as linear in decibels per degree ($[\mathrm{dB}/1^\circ]$) (see [7] and [8]). Based on simple modeling and decay rate measurements, global correction (see [9] and [10]) and manual class-based correction methods (see [2], [11], and [12]) have become the standard mitigation approaches. These approaches, although useful, have their limitations. Global corrections account for part of the effect, but as they do not consider the specifics of each area, they will ultimately undercorrect some areas while overcorrecting others. In contrast, manual corrections have the obvious disadvantage of being time-consuming and requiring significant involvement of a human operator. Additionally, in the case of nonflat areas, local topography must also be accounted for, as it plays a more important role than the instrument incidence angle to the geoid (see [13] and [14]). Overall, existing approaches could be enhanced by an automatic manner of accounting for different decay rates in a single scene. The authors of [15] seem to be the only ones to have explored this avenue, but their approach is limited to a fixed scenario and has since not been extended.

We introduce a new segmentation approach constructed by merging theoretical aspects and empirical observations into a statistical model that accounts for the incidence angle effect by assuming nonstationary per-segment means. We present the simplest functional form of the model, assuming Gaussian distributed log-intensities with linearly varying means. This model is then integrated into an already established automatic segmentation framework based on statistical mixtures. This article builds on [16], where the concept was initially introduced. We show how the approach eliminates incidence-angle-related

Manuscript received July 15, 2019; revised December 19, 2019; accepted April 20, 2020. Date of publication May 28, 2020; date of current version June 16, 2020. This work was supported in part by the Akademiaavtale between Statoil and the Arctic University of Norway and in part by CIRFA partners and the Research Council of Norway under Grant 237906. *(Corresponding author: Anca Cristea.)*

Anca Cristea and Anthony P. Doulgeris are with the University of Tromsø—The Arctic University of Norway, 9037 Tromsø, Norway (e-mail: anca.cristea.new@gmail.com; anthony.p.doulgeris@uit.no).

Jeroen van Houtte is with the Imec-Vision Lab, University of Antwerp, 2610 Antwerp, Belgium (e-mail: jeroen.vanhoutte@uantwerpen.be).

Digital Object Identifier 10.1109/JSTARS.2020.2993067

segmentation artefacts in wide-swath scenes from three sensors (Sentinel-1, Radarsat-2, and UAVSAR). The scenes were selected to include flat areas clearly exhibiting a smooth systematic decay with incidence angle: open water, sea ice, and oil slicks. With the help of remote sensing experts and overlapping optical data, we performed a visual segment validation. However, the results and discussion are based entirely on the unsupervised approach, as the supervised implementation of the same model (the classification) represents another topic and is treated in a parallel study. In addition to performing segmentation, the algorithm delivers estimates of the per-segment log-linear decay rates. We show that these estimates carry a physical meaning and can contribute to the interpretation of the obtained segments. The decays for the same target can vary between datasets acquired in different frequency bands or modes (due to sensitivity to wavelength, as well as calibration); therefore, the possibility of estimating them automatically constitutes an additional advantage. From a computational point of view, the segmentation task can be performed in a matter of minutes on typical wide-swath images, thus proving particularly useful for the sea ice and oil spill monitoring communities who require operational near-real-time algorithms.

The presented model was designed with sea ice and oil spill monitoring in mind, as they represent vast subdomains of Earth observation with important applications in both academia and industry. Nevertheless, the model is a general-purpose one and can be applied to other environments, provided that the analyzed regions are composed of relatively flat areas with predominant surface scattering. Targets that exhibit nonlinear decays remain to be studied, and if their decays can be modeled consistently, they can be incorporated into the model.

II. Methods

A. Modeling the Incidence Angle Effect

The SAR remote sensing community has tackled the incidence angle-dependent backscatter by employing various correction strategies. As the dependence is strongly related to surface scattering (see [1] and [17]), it is often treated as an illumination problem by using models adapted from optical remote sensing. At the core of this class of models stands Lambert's cosine law (see [1]), which states that radiant intensities depend linearly on the cosine of the incidence angle. The same principle applies to the observed intensities, and as the incidence and viewing angles are the same for SAR, the corresponding law for a monostatic setup relates the intensities to the square of the cosine (see [12]). However, this assumption is often too simplistic as it only applies to ideally diffusive (Lambertian) surfaces that appear uniformly bright from all directions of observation. For surfaces with different scattering properties, focus has shifted to the exploration of more general models. The Minnaert model [18] attempts to account for these differences by incorporating a surface-specific exponent k into the cosine law. k measures deviation from a perfectly diffuse reflector and depends on surface roughness: the rougher the surface, the lower its value and the slower the decay. The Minnaert model has been applied extensively in optical remote sensing for the correction of topographic effects (see [19]), and to a smaller extent in SAR imaging for vegetation studies (see [2] and [20]). Even if it does not fit every given case, it introduces the important concept of considering different incidence angle dependencies per surface.

An alternative approach to studying the incidence angle effect is estimating backscatter over smooth surfaces that exhibit small periodic perturbations, using variants of the Bragg model. In [21], theoretical curves computed using the tilted Bragg model are shown to fit backscatter measurements over open water and different types of oil slicks reasonably well. The authors of [1] report backscatter measurements for various types of surfaces and conditions, exhibiting linear, exponential, or more complicated incidence angle dependencies.

The more complicated modeling options are sometimes reduced to an empirical approximation, the exponential decay of the mean intensity $\bar{I}$ with incidence angle, as

$$\bar{I}(\theta_i) = \bar{I}_0 e^{-\frac{\theta_i}{c}} \tag{1}$$

where θ_i is the incidence angle, $\bar{I}_0$ is the mean intensity at $\theta = 0$, and c is a surface-specific constant. The exponential decay of intensities implies the linear decay of log-intensities, a practical simplification used in recent studies (see [7], [9], [11], and [22])

$$\bar{I}_{\mathrm{dB}}(\theta_i) = a - b\theta_i \tag{2}$$

where $\bar{I}_{\mathrm{dB}} = 10\log_{10}\bar{I}$, the intercept $a = 10\log_{10}\bar{I}_0$ is the mean log-intensity at an angle $\theta_0 = 0^\circ$, and the slope $b = 10/c\ln 10$ is the intensity decay rate in dB/1°. Note that we explicitly specify the decay with a negative sign and use a positive decay rate. Alternative conventions use a plus sign and negative decay rates. Using this simplification, it is possible to measure decay rates per degree for open water (see [9]) and different types of sea ice in the Arctic area throughout the year (see [7] and [22]). The simplicity of the linear decay and its demonstrated applicability to arctic scenarios make it an ideal candidate for integration into the new statistical model.

B. Existing Segmentation Framework

Our in-house automatic unsupervised SAR image segmentation framework is summarized here. The common principle consists of using statistical mixtures to model the ensemble of (multilooked) intensities or polarimetric features. Commonly used models have ranged from a simple mixture of Gaussian distributions (see [23]) to variations using more complicated textured models (see [24] and [25]). The framework itself has been successively upgraded, with its latest form having been described in detail in [25]. The previously cited works have focused on polarimetric features for relatively narrow-swath images, where the incidence angle effect is not a major concern and is essentially ignored. In this work, we only consider the log-intensities as features, as their decays with incidence angle have been studied and are known to be approximately linear [see (2)] for a variety of targets.

The base algorithm has two stages: the Gaussian-mixture-based clustering and the Markov random field (MRF)-based contextual smoothing (see [25]). We will refer to the results of the first stage as clusters, and to the final results as segments.

Clustering is performed iteratively and on two levels. At the "model selection" level, goodness-of-fit (GoF) testing and cluster splitting are performed. At the second level, mixture fitting is performed by expectation–maximization (EM) (see [26]). A consistent clustering initialization is achieved by always starting with a single cluster, which will subsequently be split until the GoF criterion is met. At the end of each EM convergence, the GoF of individual clusters is tested using Pearson's chi-squared test; then, the least well-fitting one is split. The clustering stops once all clusters are considered as good fits to a chosen sensitivity (or confidence level). Finally, hard cluster labels are assigned to all image pixels, according to their associated maximum posterior probabilities. In the second stage, MRF-based contextual smoothing can be applied if more spatially homogeneous segments are desired, while generating new posterior labels. In general, the contextual smoothing reduces clustering errors by relabeling misclassified isolated pixels, but it may also amplify them in cases where the misclassified pixels are adjacent. During this stage, the class label image is modeled as an MRF together with an isotropic second-order neighborhood system. Based on the intensity distributions, the global class prior probabilities are replaced with spatially varying local prior probabilities determined from the local neighborhoods. This stage is more computationally intensive, as it is necessary to consider all pixels.

The automatic characteristic of the algorithm refers to its capacity to determine the suitable number of clusters based on the input data, the number of samples used for clustering, and the chosen confidence level for Pearson's test. A uniformly subsampled subset of the total image pixels is used for clustering, with the dual purpose of reducing the processing time and the number of identifiable clusters. Using a low number of samples leads to the identification of only a few major well-represented clusters and thus simplifies result interpretation. As the sample number is increased, less-well-represented clusters also become identifiable, and more image details become visible. The sample number must, therefore, be adjusted empirically for each task, together with the confidence level (usually set to 99%).

C. Nonstationary Statistical Model for Log-Intensities

Intensity-based segmentation of SAR images is grounded in the assumption that intensities follow a certain statistical model based on the stochastic representation of a known physical process (here, scattering). Commonly used models account for measurable factors such as average brightness, speckle variance, and texture (see [25]), but do not account for the incidence angle. As a consequence, the systematic decay of intensities resulting from backscatter by a single target may instead appear as brightness variation, causing the respective target to be incorrectly split into multiple segments in the range dimension. An illustration of this phenomenon is given in Fig. 1, using a dual-channel wide-swath scene containing two main targets: water and sea ice. In the copolarized (HH) channel, the water intensity values cover roughly the entire dynamic range of the image, whereas the ice intensity values show a lower spread and considerable overlap with the water intensities [see Fig. 1(a) and (c)]. The effect is also present in the cross-polarized (HV) channel, although it is less pronounced [see Fig. 1(b) and (d)], because of the reduced contribution from surface scattering. When the incidence angle is added as an extra histogram dimension, the data form tubular shapes with roughly Gaussian profiles and different orientations per cluster and channel [see Fig. 1(e) and (f)]. The different decay rates become more evident when visualizing the data corresponding to the two targets separately [see Fig. 1(g) and (h): open water in green and sea ice in red]. Some overlap is present in both polarized channels (usually at different angle values), but their joint use may resolve such ambiguities. In the given example, maximum data overlap in the HH log-intensity versus incidence angle space is observed around $\theta = 37^\circ$. However, the data are clearly separated in the joint HH and HV log-intensity space at $\theta = 37^\circ$ [see Fig. 1(i)]. These observations motivate the necessity to formulate a model that includes incidence angle information.

The proposed model is based on a multivariate Gaussian mixture, where the incidence angle modulates the mean value of each component in the joint space of log-intensities (x) and incidence angles (θ). In other words, the mixture components (clusters) are assumed to follow multivariate Gaussian distributions along constant incidence angle azimuth lines, with mean values expressed as a linear function of the corresponding incidence angles. Multidimensionality relates to the existence of multiple (d) polarimetric channels. We implement the different per-cluster and per-channel incidence angle dependencies by considering d-dimensional parameter vectors for each cluster k: $\mathbf{a}_k$ represents the mean value [dB] at $\theta = 0^\circ$ and $\mathbf{b}_k$ represents the decay rate [dB/1°]. The two parameters correspond to the intercept and slope, respectively, from (2). The covariances $\mathbf{\Sigma}_k$ are assumed to be constant with respect to the incidence angle. The concept can thus be interpreted as a Gaussian distribution "shifted" along the range dimension. After including the prior weights π_k, the M-component mixture becomes

$$p_{X,\Theta}(\mathbf{x},\theta) = \sum_{k=1}^{M} \pi_k \frac{1}{(2\pi)^{d/2}|\mathbf{\Sigma_k}|^{1/2}} \times \exp\left(-\frac{1}{2}(\mathbf{x}-(\mathbf{a_k}-\mathbf{b_k}\theta))^T \mathbf{\Sigma_k}^{-1}(\mathbf{x}-(\mathbf{a_k}-\mathbf{b_k}\theta))\right). \tag{3}$$

Mixture separation is conducted using the EM algorithm. The expectation step represents the computation of the component membership weights per sample, expressed as posterior probabilities. If $\mathcal{N}(\mathbf{x_k};\mathbf{a_k}-\mathbf{b_k}\theta_i,\mathbf{\Sigma_k})$ denotes the Gaussian (Normal) likelihood that the sample $(\mathbf{x_i},\theta_i)$ belongs to component k, then the posterior probability that the same sample $(\mathbf{x}_i,\theta_i)$ belongs to the component k is

$$z_{ik} = \frac{\pi_k \mathcal{N}(\mathbf{x_i};\mathbf{a_k}-\mathbf{b_k}\theta_i,\mathbf{\Sigma_k})}{\sum_{j=1}^{M}\pi_j \mathcal{N}(\mathbf{x_i};\mathbf{a_j}-\mathbf{b_j}\theta_i,\mathbf{\Sigma_j})}. \tag{4}$$

The maximization step consists of estimating the parameter values that maximize the total likelihood given the previously

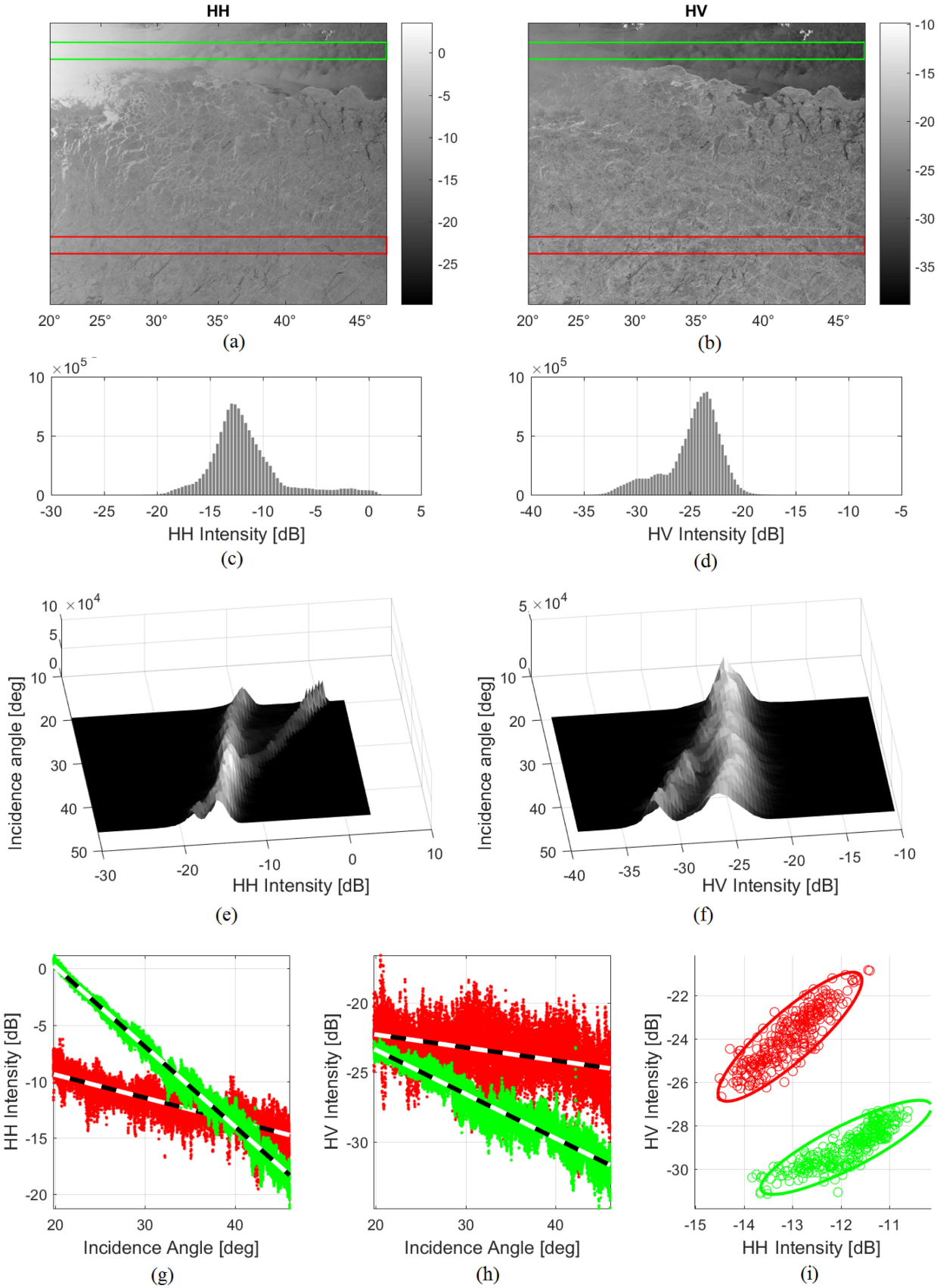

Fig. 1. Scene 1 (Sentinel-1 EW mode): (a) and (b) log-intensities and selected regions of open water (green, top) and sea ice (red, bottom), (c) and (d) global log-intensity histograms, and (e) and (f) global log-intensity versus incidence angle histograms. Representation of the selected open water and sea ice regions: (g) and (h) log-intensity decay rates with incidence angle and linear model lines, (i) log-intensities and 95% confidence ellipses corresponding to Gaussian model fits at $\theta = 37°$. (g) and (i) show how data overlap in two of the feature spaces can be resolved in the third feature space.

TABLE I
SUMMARY OF THE SCENE CHARACTERISTICS

Scene #	Sensor	Mode	Coverage (km)	Date of acquisition	Incidence angles (°)	Nominal number of looks	Resolution (m)
1	Sentinel-1	Extra Wide (EW)	400 x 400	27/11/2015	$19-47$	6x3 (EW 1), 6x2 (EW 2-5)	20 x 40
2	Sentinel-1	Extra Wide (EW)	400 x 400	28/11/2015	$19-47$	6x3 (EW 1), 6x2 (EW 2-5)	20 x 40
3	Radarsat-2	ScanSAR Wide A (SCWA)	500 x 500	10/01/2015	$20-49$	6x2	100 x 100
4	UAVSAR	PolSAR	20 (swath)	11/06/2015	$20-70$	1x1	2 (range, single-look)
5	UAVSAR	PolSAR	20 (swath)	11/06/2015	$20-70$	1x1	2 (range, single-look)
6	Sentinel-1	Extra Wide (EW)	400 x 400	04/04/2016	$19-47$	6x3 (EW 1), 6x2 (EW 2-5)	20 x 40
7	Landsat-8	-	180 x180	04/04/2016	-	-	30 x 30

computed membership weights. In this case, closed-form expressions are obtained for all four model parameters, i.e.,

$$\pi_k = \frac{\sum_{i=1}^{n} z_{ik}}{\sum_{j=1}^{M}\sum_{i=1}^{n} z_{ij}} \tag{5}$$

$$\mathbf{a_k} = \frac{\sum_{i=1}^{n} z_{ik}\mathbf{x_i} + \mathbf{b_k}\sum_{i=1}^{n} z_{ik}\theta_i}{\sum_{i=1}^{n} z_{ik}} \tag{6}$$

$$\mathbf{b_k} = \frac{-\sum_{i=1}^{n} z_{ik}\theta_i\mathbf{x_k} + \mathbf{a_k}\sum_{i=1}^{n} z_{ik}\theta_i}{\sum_{i=1}^{n} z_{ik}\theta_i^2} \tag{7}$$

$$\mathbf{\Sigma_k} = \frac{\sum_{i=1}^{n} z_{ik}(\mathbf{x_i} - (\mathbf{a_k} - \mathbf{b_k}\theta_i))(\mathbf{x_i} - (\mathbf{a_k} - \mathbf{b_k}\theta_i))^T}{\sum_{i=1}^{n} z_{ik}}. \tag{8}$$

The above describe our prototype approach to introducing nonstationarity with respect to incidence angle in the statistics of SAR images. Imprecision due to simplistic modeling can be corrected in the future by assuming statistical models with an increased level of complexity and nonlinear decay rates. The simple prototype is sufficient to demonstrate functionality, while also bypassing complex calculations and long runtimes.

III. DATA PREPROCESSING AND DESIGN OF DEMONSTRATIONS

We have conducted four demonstrations in order to highlight the improvements obtained when using the proposed model for segmentation, the consistency of the results upon application on scenes from different sensors, the possibility to identify structures associated with the obtained segments on optical data, and the potential of using estimated log-linear decay rates for ice–water mapping. We have selected six SAR scenes and one optical scene (see Table I) for these demonstrations. The SAR scenes were acquired over wide swaths and contain flat distributed targets presenting predominant surface scattering, the type that are known to display log-linear intensity decays. The satellite scenes depict arctic scenarios typical for sea ice monitoring, i.e., open water and sea ice subtypes (see Fig. 3), and were selected with the purpose of illustrating similar algorithm behavior on scenes with similar compositions from two different sensors. The UAVSAR scenes were acquired in the North Sea during the NORSE2015 oil spill exercise (see [27]) and contain oil slicks on an open water background. We note that the grayscale representations of the HH and, respectively, HV log-intensities are always visualized from near to far range, thus making the scenes acquired in ascending orbits appear inverted in comparison to the geolocated ones from Fig. 3. Finally, the Landsat-8 scene was selected due to its good spatial and temporal overlap with Sentinel-1 scene 6 (see Table I).

The Sentinel-1 and Radarsat-2 satellite scenes were processed using the same protocol. First, thermal noise removal was applied to the original products by subtracting the noise equivalent sigma zero (NESZ) profiles provided in the metadata. This is an important step, as both satellites have irregular NESZ profiles. It must nevertheless be noted that the provided profiles are not perfectly estimated, and residual noise is still present after correction, especially for the Sentinel-1 Extra-Wide (EW) mode data. More specifically, this acquisition mode presents two types of problematic artefacts. First, the image construction process involves a step where five acquisition strips affected by different thermal noise levels are stitched together into a final image, resulting in visible stitching boundaries and variable noise-floor patterns in the range direction. Second, the TOPSAR technique used in the EW mode (see [28]) introduces a scalloping effect in the azimuth direction, which also varies between strips (see [29]). The descalloping function used to correct this effect then further amplifies the noise at the beam edges. Both artefacts are more visible in the HV channel, because of weaker backscatter and lower signal-to-noise ratio. Out of the two selected examples, Scene 1 does not exhibit obvious noise patterns because of the high brightness of the targets, whereas Scene 2 represents a more typical case dominated by dark areas and visible noise. The corrected images were radiometrically calibrated to Sigma Nought using ESAs Sentinel Application Platform. Smoothing was applied using an averaging 5×5

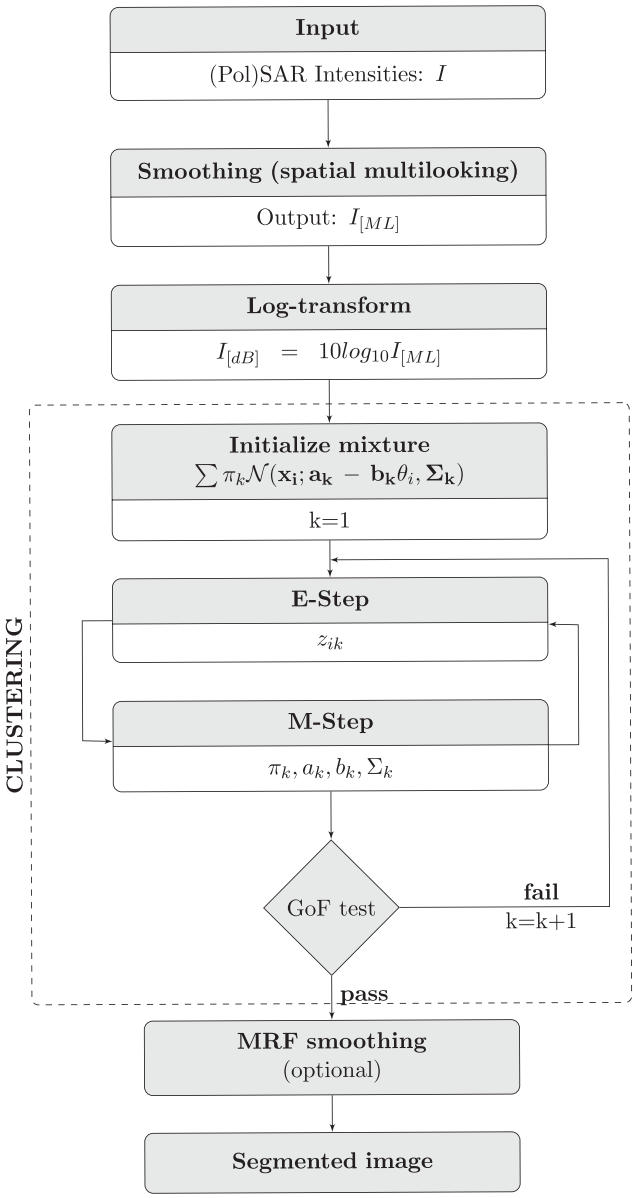

Fig. 2. Workflow diagram illustration of the main image preprocessing and segmentation steps, including the two EM steps (E-step and M-step), GoF test, and MRF-based smoothing.

pixel window in order to reduce data spread and thus increase cluster radiometric separability. Next, the size of the images was reduced by subsampling at a 5×5 rate in range and azimuth. Finally, the intensities were log-transformed, this step being essential for ensuring both that the data are approximately Gaussian distributed and that the decay is linear. Prior to segmentation, the original product land masks were applied, as land topography is more complicated than a flat surface, and intensities do not follow the expected log-linear decay with respect to the geoid angle.

The UAVSAR polarimetric data are available in single-look complex format and incorporates radiometric calibration. In addition, the UAVSAR instrument's NESZ is low (varying between approximately -55 and -40 dB across the range according to [21, Appendix A]), much lower than the NESZ of approximately -22 dB of the two satellites. The acquired signal values were situated above this limit; therefore, noise correction was not necessary. The preprocessing of UAVSAR scenes was reduced to spatial multilooking (using a 15×60 pixel window), subsampling (at a 15×60 rate), and log-transformation. Segmentation was applied only to the HH intensities in the 30–60° range, where log-linear decays were observed. The remaining channels exhibited irregular decays. The same dataset is used in [30], where it is reported that the data collected over water were not corrected for crosstalk in the cross-polarized channels. The irregular decays can, therefore, be explained by imperfect calibration, at least in the cross-polarized channels. Discussions with co-authors of the study describing UAVSAR calibration (see [31]) confirmed that the procedure has since improved.

The preprocessing steps common to all scenes (spatial multilooking and log-transformation) as well as the main algorithm steps are summarized in Fig. 2.

A. Demonstration 1: Improving Wide-Swath Image Segmentation

We demonstrate the improved segmentation results using two examples.

For the first example, we use Scene 1 (see Figs. 1(a), (b) and 3) to conduct a comparison between three segmentation strategies: segmenting using a Gaussian mixture model, applying a global correction (based on one mean decay rate) before segmenting using the same Gaussian mixture model, and segmenting using the proposed nonstationary mixture model. The applied global correction is based on the mean decay rate considering all intensity values and is, therefore, expected to undercorrect areas with steep decays and overcorrect areas with flatter decays. Here, these correspond to the open water areas and the ice areas, respectively, owing to the differences in roughness. We note that since the method is unsupervised, the segments need further assessment in order to be assigned physically meaningful labels, i.e., become "classes." A thorough validation of each segment was not performed, as we lack the ground truth to verify the profile of certain regions, and only segments that were considered clear to interpret by visual inspection by sea ice experts were referred to as water or ice.

The second example has the additional purpose of showing the effect of noise on the segmentation. We use Scene 2 [see Figs. 3 and 5(a) and (b)], where the noise artefacts are still noticeable after thermal noise correction. We compare the segmentation results obtained when using the Gaussian mixture model and the new nonstationary mixture model.

B. Demonstration 2: Multisensor Reproducibility

The second demonstration focuses on the applicability of the proposed model for the segmentation, using three scenes from different sensors: Radarsat-2 and UAVSAR. All three scenes were segmented using the Gaussian mixture model and the nonstationary mixture model, for comparison. Like in the first demonstration, the segments obtained from the satellite scene were only validated by visual inspection. As the UAVSAR

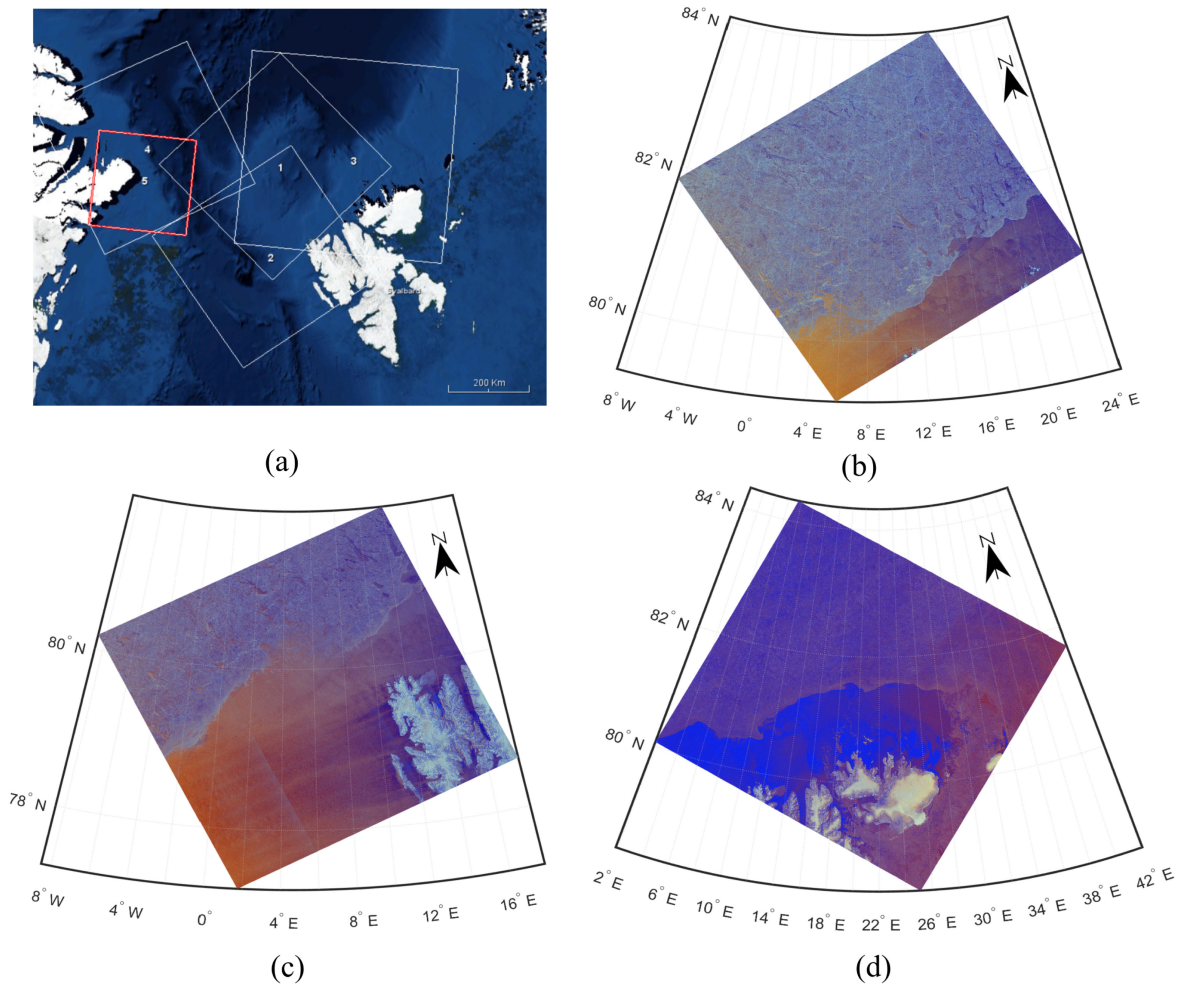

Fig. 3. (a) Locations of the five satellite scenes used in the article: 1, 2, and 4: Sentinel-1 EW mode (Copernicus Sentinel data [2015, 2016]), 3: Radarsat-2 SCWA mode, and 5: Landsat-8. False-color representations [HH(R), HV(G), and HV/HH(B)] of the SAR scenes used to demonstrate full-image segmentation, using WGS84 coordinates: (b) Scene 1. (c) Scene 2. (d) Scene 3. Scenes 4 and 5 have partial overlap, displayed in Fig. 9.

scenes were acquired during a controlled exercise, their compositions are known precisely, and the validation of the obtained segments is straightforward.

C. Demonstration 3: Comparison With Overlapping Optical Data

We present an example of overlapping Sentinel-1 and Landsat-8 scenes, both acquired during spring when illumination is not an issue for the optical sensor. The example is meant to serve as an indication that the proposed algorithm can identify visible structures, even if it is not a full-on validation with *in situ* information. The overlapping region covers the incidence angles from approximately 23° to 37° in the SAR scene and contains sea ice, which is covered by snow in the optical scene, and leads that are sometimes covered by thin ice, which are identifiable in both scenes (see Fig. 9). Because the optical image and the SAR image are different in nature, we can only make statements about the structures that have well-identifiable signatures in both images. The Sentinel-1 SAR scene and the Landsat-8 optical scene (scenes 6 and 7 in Table I) are acquired at 16:35 and 15:39, respectively, and an examination of the superimposed images showed no differences in the positions of the leads within the ice mass. The segmentation was performed using clustering alone, but using a higher number of samples than in the other cases, in order to better capture the details of the fine leads. The MRF-based smoothing stage was skipped in order to avoid any resulting ambiguity.

D. Demonstration 4: Ice–Water Distinction

Ice–water mapping is a high-interest topic for operational services and is currently being investigated using various strategies often based on local pixel statistics (see [32]) and locally computed polarimetric features (see [8] and [33]). The incidence angle effect is typically no less of a nuisance for this task than it is for segmentation, but we now have the tool to transform it into a source of physically significant information, as our segmentation algorithm also estimates segment features, i.e., the slope (log-intensity decay rate), intercept, and covariance. Among these features, the HH log-intensity slope is of particular interest, as it is sensitive to roughness and could, therefore, help distinguish ice and water based on their roughness, i.e., act as a feature for ice–water mapping. In this demonstration, we show that

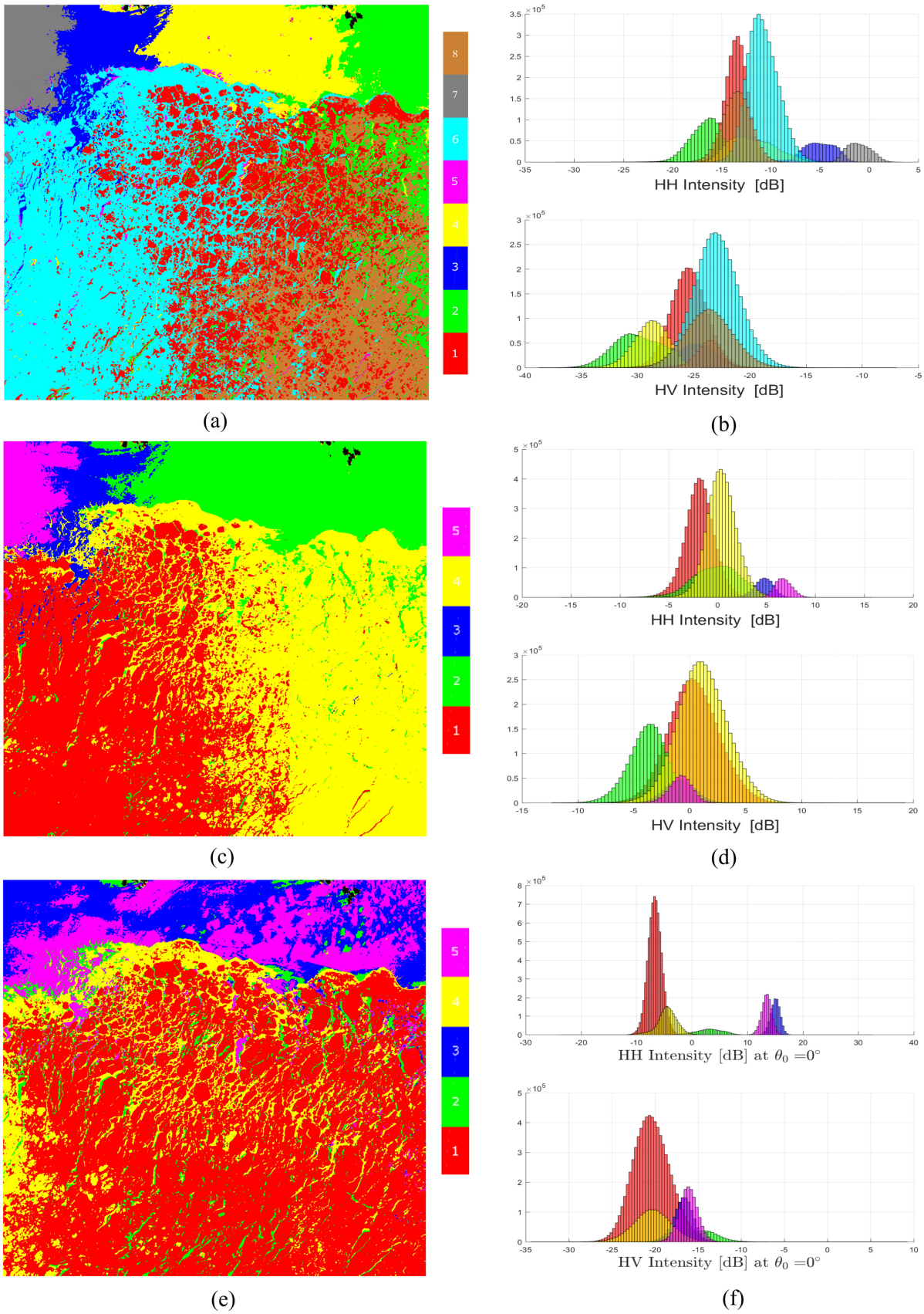

Fig. 4. Scene 1 (Sentinel-1 EW mode): comparison of the segmentation results and segment histograms obtained after applying: (a) and (b) the Gaussian mixture model, (c) and (d) a global correction and the Gaussian mixture model, and (e) and (f) the proposed nonstationary mixture model. Results from the three approaches show incremental improvement of across-range segment connectivity and class distinction. Land masked out in black.

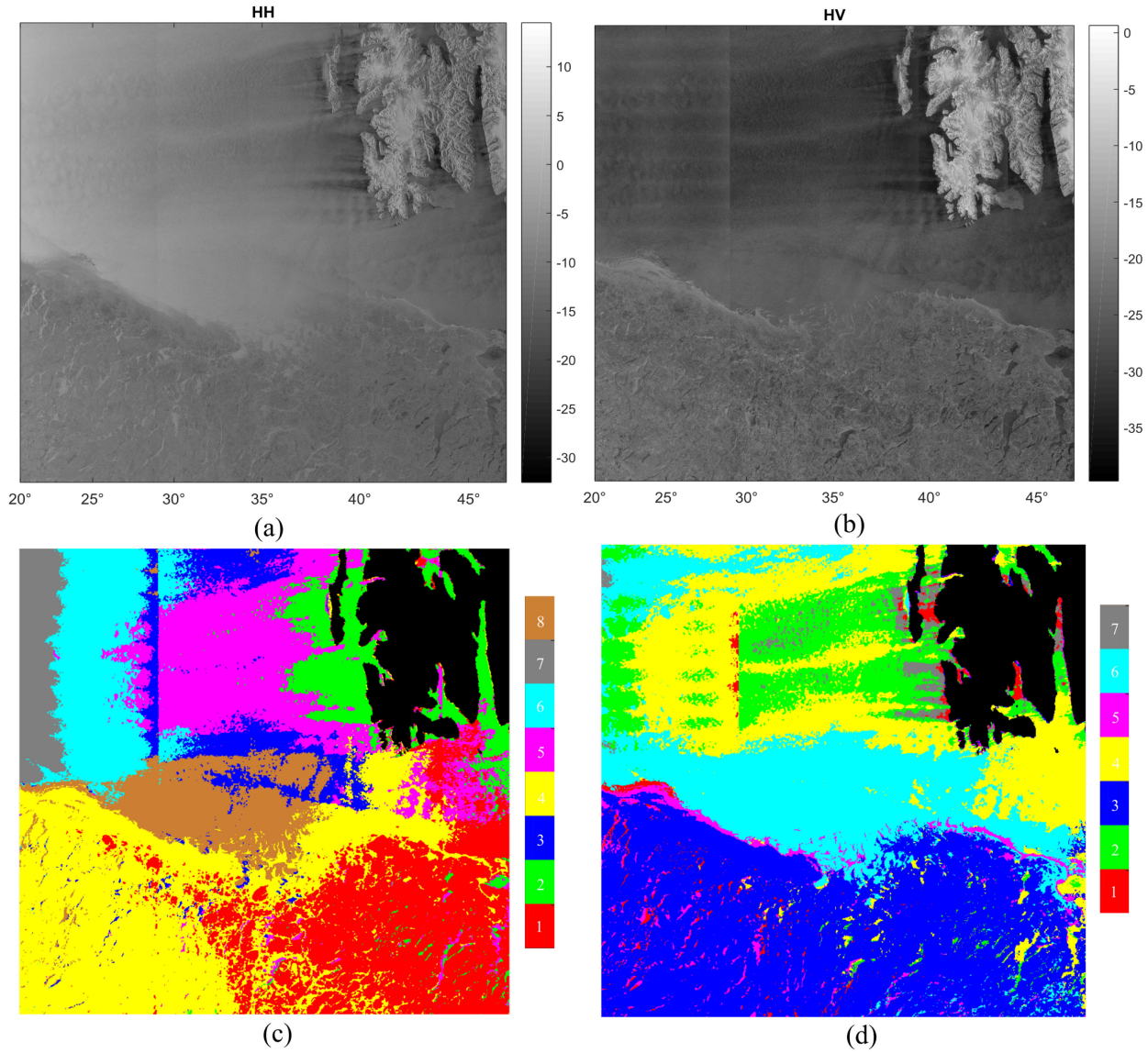

Fig. 5. Scene 2 (Sentinel-1 EW mode): (a) and (b) log-intensities; comparison of the segmentation results obtained after applying (c) the Gaussian mixture model, and (d) the proposed nonstationary mixture model. Application of the nonstationary model leads to connected segments, despite the visible residual noise artefacts. Land masked out in black.

ice–water distinction may be achieved by using the slope alone, while also discussing potential limitations. After conducting a comparison between slope values reported in previous studies (see [7] and [22]) and our own measurements, we selected an appropriate threshold value to distinguish between water and ice. The previously segmented satellite images were then relabeled as "ice" or "water" according to this threshold.

IV. Results and Discussion

A. Demonstration 1: Improving Wide-Swath Image Segmentation

Fig. 4 shows the results obtained after applying each of the three segmentation approaches on Scene 1. Using a Gaussian mixture model led to oversegmentation into multiple bands in the range dimension [see Fig. 4(a)]. Histogram overlap illustrated statistical ambiguities [see Fig. 4(b)]. The application of a single-rate correction followed by Gaussian-mixture-based segmentation resulted in fewer bands and less overlap compared to the first case, but the segments were still not connected throughout the entire range [see Fig. 4(c)]. The limited efficiency of the global correction was expected, as the two major targets present in the scene have very different decay rates. Finally, considering the per-cluster incidence angle dependencies produced connected segments [see Fig. 4(e)], proving that the nonstationary model is better fitting. A representation of the data distribution using projections at a single incidence angle also illustrated the expected Gaussian profiles, and the projection at $\theta = 0^\circ$ showed minimal overlap, notably in the HH channel [see Fig. 4(d)].

According to visual inspection by sea ice experts, the high backscatter in the near range of the open water area suggests the presence of wind, while some alternating intensity levels

on the water surface and in the ice leads (at similar incidence angle values) also suggest the presence of different wind regimes (see [34] and [35]). The segments obtained with the proposed model [see Fig. 4(e)] offered the most detail in terms of identifiable structures: water areas (segments 3 and 5), sea ice (segment 1), and mixtures of sea ice and leads (segments 2 and 4).

The segmented Scene 2 [see Fig. 5(a) and (b)] was visibly affected by both types of noise artefacts, stitching boundaries, and scalloping, regardless of the model [see Fig. 5(c) and (d)]. As the noise problems are not addressed by either model, this outcome was expected. Nevertheless, when the nonstationary model was employed, segment connectivity was maintained despite the artefacts [in Fig. 5(d)]. According to visual validation, segment 3 covers a large ice floe, and segments 2 and 4 appear to cover water regions with different wind regimes. The area corresponding to segment 6 has the aspect of open water or grease ice, but this information contains some uncertainty. While this result confirms the utility of the proposed model, it also reiterates the need for reliable noise-correction procedures. Noise correction could potentially be achieved during segmentation, by simultaneously estimating the linear decays and variable noise floor for each cluster.

B. Demonstration 2: Multisensor Reproducibility

Scenes 3–5 (from Radarsat-2 and UAVSAR) exhibit the same statistical properties and incidence angle-dependencies as the Sentinel-1 scenes. As a result, segmenting the Radarsat-2 scene [see Fig. 6(a) and (b)] without considering the incidence angle led to banding in the range dimension [see Fig. 6(c) and (d)], although the effect was less pronounced compared to the Sentinel-1 scenes. This is due to the scene being dominated by sea ice, which exhibits slower intensity decays than water. Applying the proposed model [see Fig. 6(e) and (f)] eliminated the banding and connected the segments throughout the range, like in the previous examples.

Scene 4 [see Fig. 7(a)] contains an oil spill that was detectable by clustering even without considering the incidence angle effect. However, banding occurred when the effect was not considered, and the oil slicks appeared to belong to the same cluster as one of the water bands [see Fig. 7(b)]. By using the current model, the banding was eliminated, and the open water regions were connected into one cluster, while different clusters were identified for the oil slicks and the previously undetected ships [see Fig. 7(d)]. The incorrectly labeled pixels from the very near range were a result of deviations from the linear approximation of the decay, which in turn were due to nonnegligible specular contributions. Scene 5 [see Fig. 8(a)] shows a series of oil spills that were not detected when using the Gaussian-mixture-based model [see Fig. 8(b)], but appeared as connected structures when using the proposed model [see Fig. 7(d)]. However, owing to a lower radiometric contrast between oil and water and thus higher statistical overlap than in Scene 4, more clustering errors were present. Adding texture and incorporating the other channels (with correctly calibrated data) may reduce such false alarms in the future. The inclusion of the entire range of incidence angles may be possible if a nonlinear decay is used, as the very near and very far range data exhibit deviations from linearity. MRF-based smoothing was not applied to the clustered UAVSAR scenes, as it did not improve result interpretation. In Scene 1, few errors were present postclustering, and smoothing would not have changed the result significantly. On the opposite side, Scene 2 contained many adjacent misclustered pixels and smoothing would have amplified the error by grouping them together.

The system used for processing is equipped with an i7 @ 2.6-GHz CPU, 16-GB RAM, and a solid-state drive and is running MATLAB on Windows. The processing time for the clustering stage of the algorithm varied slightly with the subsampling rate, but did not exceed 1 min for the examples presented in this article (or similar ones). The smoothing stage for the same scenes took on average under 5 min.

Overall, segmenting using the nonstationary model was effective for all scenes, thus confirming its applicability for both large-scale environmental monitoring from satellites and targeted UAVSAR missions.

C. Demonstration 3: Comparison With Overlapping Optical Data

The overlapping fragments of the Sentinel-1 and Landsat-8 scenes (Scenes 6 and 7 in Table I) as well as the segmentation result from the SAR scene fragment are shown in Fig. 9. We have highlighted the segments corresponding to the open water/leads (red) and the thin ice-covered leads (green). In the case of very thin leads, some ambiguity is observed between the two lead types, likely because the concerned intensity values lie in the overlapping region of the respective clusters. The remainder of the image contains snow-covered ice that cannot be detected in the optical image, but the varying backscatter in the SAR image indicates the presence of multiple ice types. In addition, due to the different resolutions (20 m by 40 m for the SAR image and 30 m for the optical image), the finer details are not captured in the SAR image.

D. Demonstration 4: Ice–Water Distinction

Based on HH log-intensity slope measurements from previous studies and on our own estimations, the value of 0.39 $\mathrm{dB}/1^{\circ}$ was selected as the threshold between ice and water. Using this threshold to relabel the previously segmented satellite images (i.e., the segments with slow decaying intensities were mapped as ice and those with fast-decaying intensities as water), we obtained the ice–water maps illustrated in Fig. 10. According to sea ice experts, the result is realistic, with some ambiguities for segments 1 and 6 of the Radarsat-2 scene [see Fig. 6(c)]. The signal from the corresponding areas was too low to be accurately measured and their slopes appeared flat; therefore, they were classified as ice. In this case, it would be necessary to introduce a constraint that excludes such areas from classification, or to jointly consider the slope and other features for a more accurate result. Nevertheless, the current example is sufficient to demonstrate the potential of the HH log-intensity slope as an interpretative feature.

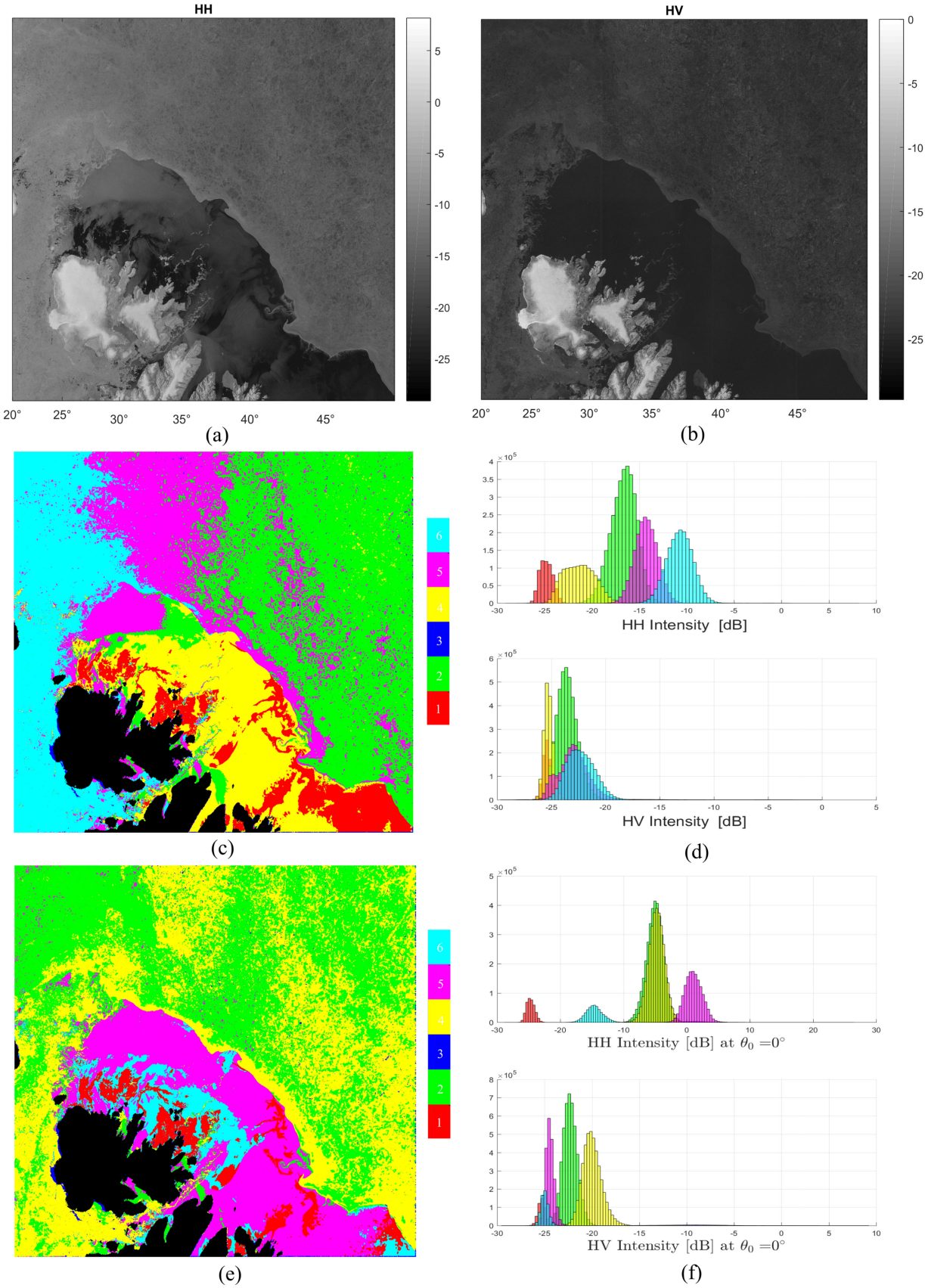

Fig. 6. Scene 3 (Radarsat-2 SCWA mode): (a) and (b) log-intensities; comparison of the segmentation results and segment histograms obtained after applying (c), and (d) the Gaussian mixture model and (e) and (f) the proposed nonstationary mixture model. Application of the nonstationary model has the same impact here as in the case of Sentinel-1 scenes (see Figs. 4 and 5). Land masked out in black.

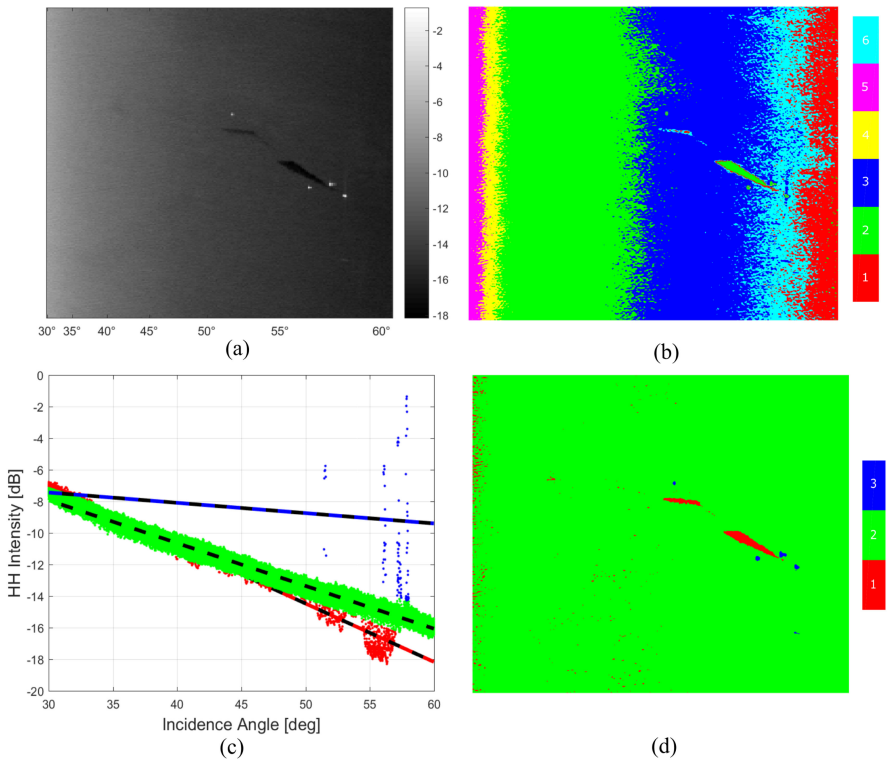

Fig. 7. Scene 4 (UAVSAR PolSAR mode): oil slicks and ships in the open sea: (a) HH intensities [dB], (b) segmentation result obtained after applying the Gaussian mixture model, (c) intensity decay rates per segment, and (d) segmentation result obtained after applying the proposed nonstationary mixture model. Application of the nonstationary model correctly segments the underlying image structures, eliminating the clear banding artefacts produced by the Gaussian mixture model.

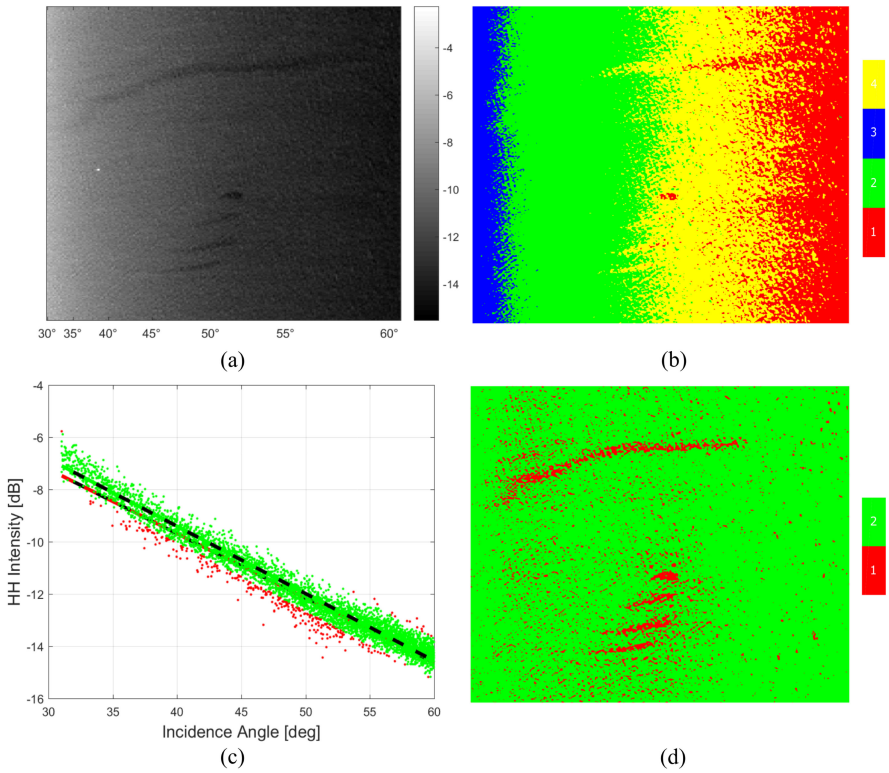

Fig. 8. Scene 5 (UAVSAR PolSAR mode) : low-contrast oil slicks in the open sea: (a) HH intensities [dB], (b) segmentation result obtained after applying the Gaussian mixture model, (c) intensity decay rates per segment, and (d) segmentation result obtained after applying the proposed nonstationary mixture model. Application of the nonstationary model identifies the oil slicks, although some segmentation errors remain because of statistical ambiguities (due to the use of only one channel).

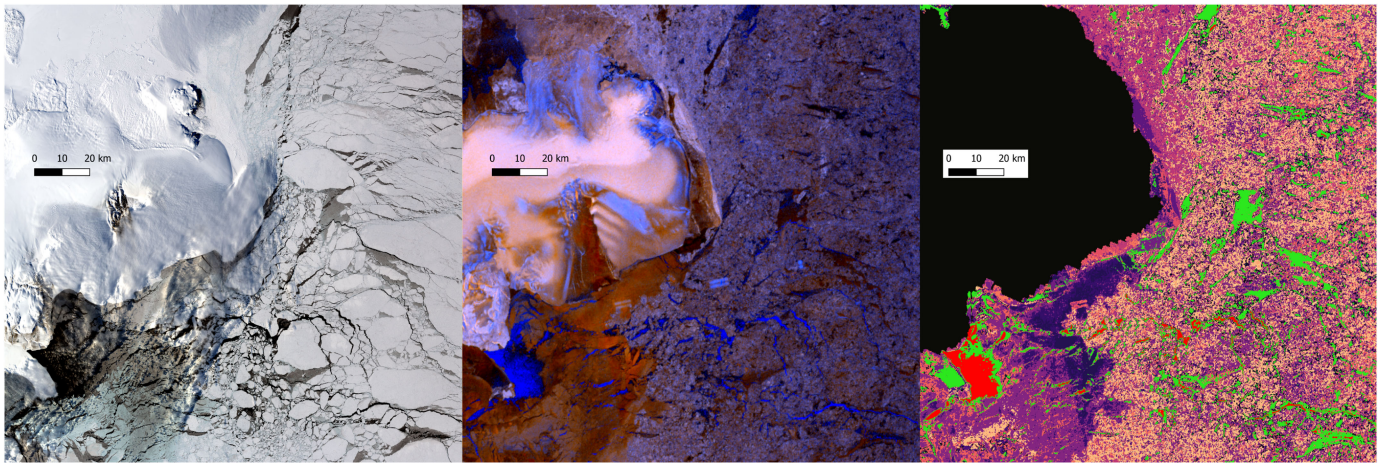

Fig. 9. Overlaping sections of (a) Scene 7 (Landsat-8 RGB). (b) Scene 6 [Sentinel-1 EW mode, false-color representation: HH(R), HV(G) and HV/HH(B)]. (c) Segmentation result obtained from the SAR scene. Color codes were preferred for simplicity: black—masked out land, red—the darkest patches (open water/leads), and green—leads covered by thin ice, the remaining segments represent different ice types that cannot be differentiated by evaluating the optical image alone.

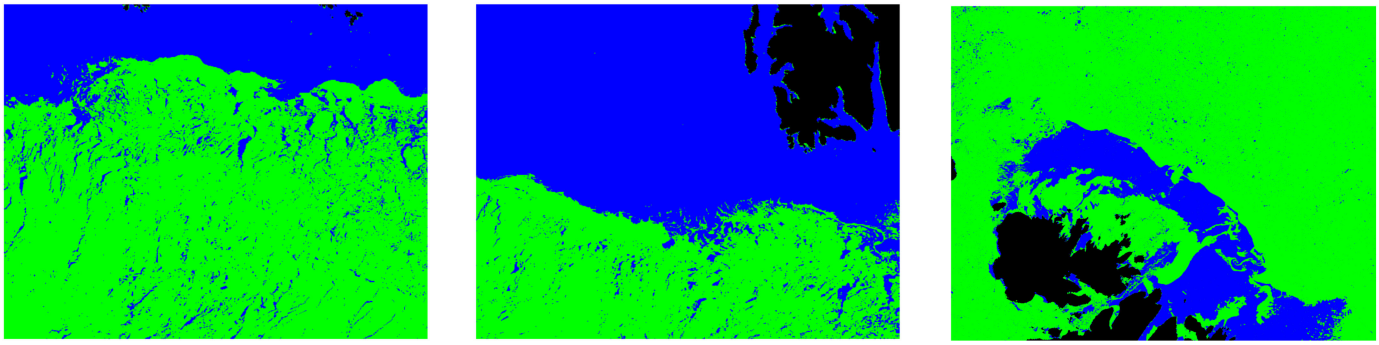

Fig. 10. Ice–water maps obtained by segmentation and thresholding of the three satellite scenes: (a) Scene 1 (Sentinel-1 EW). (b) Scene 2 (Sentinel-1 EW). (c) Scene 3 (Radarsat-2 SCWA). Blue: water and green: ice.

V. Conclusion

This article presents a new approach for the automatic segmentation of wide-swath SAR images. The approach consists in integrating the per-segment incidence angle dependence into the statistical model by considering nonstationary means. To our knowledge, this concept has not been demonstrated in other works. The resulting model was integrated into an automatic unsupervised segmentation algorithm and can be applied on a scene without requiring prior information about its content. Furthermore, a nonstationary statistical model can be applied to all SAR systems, regardless of frequency (here demonstrated on L-band UAVSAR and C-band satellites) or polarization. The approach delivers the expected results, effectively connecting segments throughout the incidence angle range, thus removing the often encountered banding artefacts that result from inadequate modeling. In addition, we demonstrated the potential of using the HH log-intensity decay rate as a feature for ice–water mapping, after showing that it is possible to effectively separate ice from water in three presegmented image examples by simply thresholding the decay rate values.

The presented method delivered good results in terms of correcting major image artefacts, and we consider that it can be further extended within this framework. We are currently exploring more complex statistical models that could account for the presence of heavy tails or texture, together with nonlinear log-intensity decay rates, which could characterize targets with different properties. The persistent noise patterns could also be corrected automatically, by introducing an adaptive model for the mean. Additional gains may be obtained by exploring the variability of polarimetric and texture features with incidence angle. The segmentation algorithm is unsupervised, but implies the possibility of performing supervised segmentation, particularly on images with limited amounts of data available at different incidence angles.

Acknowledgment

The authors would like to thank NASA/JPL-Caltech for providing the UAVSAR data and the Canadian Space Agency for the RADARSAT-2 data. The Sentinel-1 scenes were acquired during the European Space Agency's @Copernicus Programme.

The authors also wish to extend special thanks to their colleagues Malin Johansson, Thomas Kræmer, Johannes Lohse, and Wolfgang Dierking for offering their scientific and technical expertise.

REFERENCES

[1] F. T. Ulaby, R. K. Moore, and A. K. Fung, *Microwave Remote Sensing: Active and Passive. Volume II—Radar Remote Sensing and Surface Scattering and Emission Theory*. Norwood, MA, USA: Artech House, 1982.

[2] J. P. Ardila, V. Tolpekin, and W. Bijker, "Angular backscatter variation in L-band ALOS ScanSAR images of tropical forest areas," *IEEE Geosci. Remote Sens. Lett.*, vol. 7, no. 4, pp. 821–825, Oct. 2010.

[3] F. T. Ulaby, G. A. Bradley, and M. C. Obson, "Microwave backscatter dependence on surface roughness, soil moisture, and soil texture: Part II—Vegetation-covered soil," *IEEE Trans. Geosci. Electron.*, vol. 17, no. 2, pp. 33–40, Oct. 1979.

[4] C. E. Livingstone, A. L. Gray, K. P. Singh, R. G. Onstott, and L. D. Arsenault, "Microwave sea-ice signatures near the onset of melt," *IEEE Trans. Geosci. Remote Sens.*, vol. GRS-25, no. 2, pp. 174–187, Mar. 1987.

[5] P. C. Dubois and T. Engman, "Measuring soil moisture with imaging radars," *IEEE Trans. Geosci. Remote Sens.*, vol. 33, no. 4, pp. 915–926, Jul. 1995.

[6] R. K. Scharien and J. J. Yackel, "Analysis of surface roughness and morphology of first-year sea ice melt ponds: Implications for microwave scattering," *IEEE Trans. Geosci. Remote Sens.*, vol. 43, no. 12, pp. 2927–2939, Dec. 2005.

[7] M. Makynen and J. Karvonen, "Incidence angle dependence of first-year sea Ice backscattering coefficient in Sentinel-1 SAR imagery over the Kara sea," *IEEE Trans. Geosci. Remote Sens.*, vol. 55, no. 11, pp. 6170–6181, Nov. 2017.

[8] N. Zakhvatkina, A. Korosov, S. Muckenhuber, S. Sandven, and M. Babiker, "Operational algorithm for ice-water classification on dual-polarized RADARSAT-2 images," *Cryosphere*, vol. 11, no. 1, pp. 33–46, 2017.

[9] K. Topouzelis and S. Singha, "Incidence angle normalization of wide swath SAR data for oceanographic applications," *Open Geosci.*, vol. 8, no. 1, pp. 450–464, 2016.

[10] H. Liu, H. Guo, and L. Zhang, "SVM-based sea ice classification using textural features and concentration from RADARSAT-2 dual-pol ScanSAR data," *IEEE J. Sel. Topics Appl. Earth Observ. Remote Sens.*, vol. 8, no. 4, pp. 1601–1613, Apr. 2015.

[11] W. Lang, P. Zhang, J. Wu, Y. Shen, and X. Yang, "Incidence angle correction of SAR sea ice data based on locally linear mapping," *IEEE Trans. Geosci. Remote Sens.*, vol. 54, no. 6, pp. 3188–3199, Jun. 2016.

[12] I. E. Mladenova, T. J. Jackson, R. Bindlish, and S. Hensley, "Incidence angle normalization of radar backscatter data," *IEEE Trans. Geosci. Remote Sens.*, vol. 51, no. 3, pp. 1791–1804, Mar. 2013.

[13] S. K. Goyal, M. S. Seyfried, and P. E. O'Neill, "Correction of surface roughness and topographic effects on airborne SAR in mountainous rangeland areas," *Remote Sens. Environ.*, vol. 67, no. 2, pp. 124–136, 1999.

[14] G. Leclerc, N. Beaulieu, and F. Bonn, "A simple method to account for topography in the radiometric correction of radar imagery," *Int. J. Remote Sens.*, vol. 22, no. 17, pp. 3553–3570, 2001.

[15] J. Karvonen, M. Simila, and M. Makynen, "An iterative incidence angle normalization algorithm for sea ice SAR images," *IEEE Int. Geosci. Remote Sens. Symp.*, 2002, vol. 3, no. C, pp. 1524–1527.

[16] A. P. Doulgeris and A. Cristea, "Incorporating incidence angle variation into SAR image segmentation," in *Proc. IEEE Int. Geosci. Remote Sens. Symp.*, 2018, pp. 8543–8546.

[17] A. Fung, *Microwave Scattering and Emission Models and Their Applications*. Norwood, MA, USA: Artech House, 1994.

[18] M. Minnaert, "The reciprocity principle in lunar photometry," *Astrophys. J.*, vol. 93, pp. 403–410, 1941.

[19] I. Sola, M. Gonzalez-Audicana, J. Alvarez-Mozos, and J. L. Torres, "Synthetic images for evaluating topographic correction algorithms," *IEEE Trans. Geosci. Remote Sens.*, vol. 52, no. 3, pp. 1799–1810, Mar. 2014.

[20] N. Baghdadi, M. Bernier, R. Gauthier, and I. Neeson, "Evaluation of C-band SAR data for wetlands mapping," *Int. J. Remote Sens.*, vol. 22, no. 1, pp. 71–88, 2001.

[21] B. Minchew, C. E. Jones, and B. Holt, "Polarimetric analysis of backscatter from the deepwater horizon oil spill using L-band synthetic aperture radar," *IEEE Trans. Geosci. Remote Sens.*, vol. 50, no. 10, pp. 3812–3830, Oct. 2012.

[22] M. S. Mahmud, T. Geldsetzer, S. E. Howell, J. J. Yackel, V. Nandan, and R. K. Scharien, "Incidence angle dependence of HH-polarized C- and L-band wintertime backscatter over arctic sea Ice," *IEEE Trans. Geosci. Remote Sens.*, vol. 56, no. 11, pp. 6686–6698, Nov. 2018.

[23] A. P. Doulgeris and T. Eltoft, "Scale mixture of gaussian modelling of polarimetric SAR data," *EURASIP J. Adv. Signal Process.*, vol. 2010, 2010, Art. no. 874592.

[24] A. P. Doulgeris, S. N. Anfinsen, and T. Eltoft, "Automated non-Gaussian clustering of polarimetric synthetic aperture radar images," *IEEE Trans. Geosci. Remote Sens.*, vol. 49, no. 10 PART 1, pp. 3665–3676, Oct. 2011.

[25] A. P. Doulgeris, "An automatic U-distribution and Markov random field segmentation algorithm for PolSAR images," *IEEE Trans. Geosci. Remote Sens.*, vol. 53, no. 4, pp. 1819–1827, Apr. 2015.

[26] A. P. Dempster, N. M. Laird, and D. B. Rubin, "Maximum likelihood from incomplete data via the EM algorithm," *J. Roy. Statist. Soc.. Ser. B*, vol. 39, no. 1, pp. 1–38, 1977.

[27] S. Skrunes, C. Brekke, C. E. Jones, and B. Holt, "A multisensor comparison of experimental oil spills in polarimetric SAR for high wind conditions," *IEEE J. Sel. Topics Appl. Earth Observ. Remote Sens.*, vol. 9, no. 11, pp. 4948–4961, Nov. 2016.

[28] F. D. Zan and A. M. Guarnieri, "TOPSAR: Terrain observation by progressive scans," *IEEE Trans. Geosci. Remote Sens.*, vol. 44, no. 9, pp. 2352–2360, Sep. 2006.

[29] S-1 Mission Performance Centre, "Thermal denoising of products generated by the S-1 IPF," issue 1.1, Eur. Space Agency, Paris, France, Tech. Rep. MPC-0392, 2017.

[30] S. Skrunes, C. Brekke, C. E. Jones, M. M. Espeseth, and B. Holt, "Effect of wind direction and incidence angle on polarimetric SAR observations of slicked and unslicked sea surfaces," *Remote Sens. Environ.*, vol. 213, no. May, pp. 73–91, 2018.

[31] A. G. Fore *et al.*, "UAVSAR polarimetric calibration," *IEEE Trans. Geosci. Remote Sens.*, vol. 53, no. 6, pp. 3481–3491, Jun. 2015.

[32] S. Ochilov and D. A. Clausi, "Operational SAR sea-ice image classification," *IEEE Trans. Geosci. Remote Sens.*, vol. 50, no. 11, pp. 4397–4408, Nov. 2012.

[33] F. Li, D. A. Clausi, L. Wang, and L. Xu, "A semi-supervised approach for ice-water classification using dual-polarization SAR satellite imagery," in *Proc. IEEE Comput. Soc. Conf. Comput. Vis. Pattern Recognit. Workshops*, pp. 28–35, 2015.

[34] W. Dierking, "Sea ice monitoring by synthetic aperture radar," *Oceanography*, vol. 26, no. 2, pp. 100–111, 2013.

[35] A. M. Johansson, C. Brekke, G. Spreen, and J. A. King, "X- , C- , and L-band SAR signatures of newly formed sea ice in Arctic leads during winter and spring," *Remote Sens. Environ.*, vol. 204, no. Oct. 2017, pp. 162–180, 2018.

Anca Cristea received the B.Sc. degree in applied electronics and M.Sc. degree in image processing from the Politehnica University of Bucharest, Bucharest, Romania, in 2010 and 2012, respectively, and the Ph.D. degree in signal and image processing from the Claude Bernard Lyon 1 University, Villeurbanne, France, in 2015.

She is currently a Postdoctoral Researcher with the University of Tromsø—The Arctic University of Norway, Tromsø, Norway. Her research has previously focused on medical ultrasound imaging, with emphasis on statistical methods for quantitative ultrasound. Her current research interests include remote sensing of the cryosphere from synthetic aperture radar.

Jeroen Van Houtte received the B.Sc. degree in physics from the University of Antwerp, Antwerp, Belgium, in 2014, and the M.Sc. degree in physics and astronomy from Ghent University, Ghent, Belgium, in 2016. He is currently working toward the Ph.D. degree with the imec-Vision Lab, University of Antwerp, for which he has cooperated with the Center for Image-Guided Therapy and Interventions, Shanghai Jiao Tong University, Shanghai, China.

From July 2015 to September 2015, he was a Visiting Student with the Wisconsin IceCube Particle Astrophysics Center, Madison, WI, USA. From August 2016 to October 2016, he performed an internship with the Earth Observation Laboratory, University of Tromsø, Tromsø, Norway. His current research interests include statistical shape modeling and image registration and segmentation techniques, in particular radiographic data.

Anthony P. Doulgeris (Senior Member, IEEE) received the B.Sc. degree in physics from The Australian National University, Canberra, ACT, Australia, in 1988, and the M.Sc. and Ph.D. degrees in physics from the Department of Physics and Technology, University of Tromsø—The Arctic University of Norway, Tromsø, Norway, in 2006, and 2011, respectively.

In 2007, he joined the Department of Physics and Technology, University of Tromsø—The Arctic University of Norway, where he is currently an Associate Professor and Head of the Earth Observation Group. His research interests focus on developing generic algorithms for remote sensing, pattern recognition, and multidimensional statistical modeling, in particular for polarimetric synthetic aperture radar applications in sea ice and glaciers.